



A quasi-three-dimensional non-isothermal dynamic model of a high-temperature proton exchange membrane fuel cell

Jaeman Park, Kyoungdoug Min*

School of Mechanical and Aerospace Engineering, Seoul National University, 1 Gwanak-ro, Gwanak-gu, Seoul 151-744, Republic of Korea

HIGHLIGHTS

- The model can predict dynamic characteristics of High-Temperature PEM Fuel Cell.
- Increased cell temperature results in enhanced fuel cell performance.
- In transient state, the second time delay is related to the MEA temperature.
- The transient response of the voltage is strongly dependent on the cell temperature.

ARTICLE INFO

Article history:

Received 9 March 2012

Received in revised form

3 May 2012

Accepted 21 May 2012

Available online 27 May 2012

Keywords:

High temperature

Polybenzimidazole

Proton exchange membrane fuel cell

Modeling

ABSTRACT

A quasi-three-dimensional non-isothermal dynamic model of a high-temperature proton exchange membrane fuel cell, operating with a polybenzimidazole membrane, has been developed. In the model, dynamic equations of energy conservation, species conservation and electrochemical reaction are solved within a simplified quasi-three-dimensional geometry. With this simplified geometry, the model can predict the distribution of fuel cell characteristics and physical phenomena in a high-temperature proton exchange membrane fuel cell during the steady and the transient states within minutes, without using a computational fluid dynamics program. The simulation results of the current–voltage polarization curve are validated with the experimental data reported in the literature. The simulation results show a good agreement with the experimental data and show that the variation of temperature strongly affects the fuel cell's performance. In particular, the simulation results show that the transient response of the cell voltage is dependent upon that of the cell temperature.

© 2012 Elsevier B.V. All rights reserved.

1. Introduction

The proton exchange membrane fuel cell (PEMFC) has been regarded as a promising clean energy source due to its high power density, rapid start-up, high efficiency and low emissions [1]. Although great advances have been made in PEMFC development, issues such as water management, thermal management, sluggish electrochemical cathode kinetics and intolerance to impurities, such as CO, remain as obstacles to commercialization for both transportation and stationary applications [2–4].

Recent progress in PEMFC technologies has focused on the need to develop PEMFCs that operate above 100 °C [4–9]. A high-temperature PEMFC (HT-PEMFC) with a polybenzimidazole (PBI) membrane, which operates in the temperature range of 120–200 °C, has many attractive features compared with typical

PEMFCs [10,11]. One of the advantages of the PBI-based HT-PEMFC is that such a system does not require humidification [12,13]. The Nafion® membrane, which is based on perfluorosulfonated polymers and is used in typical PEMFCs with an operating temperature range of 50–80 °C, requires a highly hydrated state to effectively conduct protons. Thus, to maintain a high water content in the cell, external humidification is required. In contrast, a PBI membrane is not dependent on water content for proton conductivity and can operate at temperatures up to 200 °C; therefore, external humidification is not required and the product's water exists primarily in the vapor phase in the cell. In addition, due to the extremely low electro-osmotic drag coefficient of the PBI membrane, water transport across the membrane is ignored [14]. Consequently, water management is no longer a problem in the HT-PEMFC [15,16]. PBI-based HT-PEMFCs have other advantages due to their high operating temperature, including improvement in the electrochemical kinetics, tolerance of the poisonous effects of CO [17] and the application of a simplified cooling system [18,19].

* Corresponding author. Tel.: +82 2 880 1661; fax: +82 2 883 0179.

E-mail address: kadmin@snu.ac.kr (K. Min).

Nomenclature

A	surface area [m^2]	Re	Reynolds number [–]
\underline{C}	solid specific heat capacity [$\text{kJ kg}^{-1} \text{K}^{-1}$]	\dot{R}	species reaction rate ($\text{H}_2, \text{H}_2\text{O}, \text{N}_2, \text{O}_2$) [kmol s^{-1}]
\bar{C}	species molar concentration ($\text{H}_2, \text{H}_2\text{O}, \text{N}_2, \text{O}_2$)	R_{dif}	diffusion resistance [$\text{m}^3 \text{s}^{-1}$]
C_V	gas constant-volume specific heat capacity [$\text{kJ kg}^{-1} \text{K}^{-1}$]	Sh	Sherwood number [–]
\bar{D}_m	diffusion coefficient [$\text{m}^2 \text{s}^{-1}$]	t	time [s], thickness [m]
D_H	hydraulic diameter [m]	T	temperature [K]
E_a	activation energy [kJ kmol^{-1}]	V	voltage [V]
F	Faraday's constant [$96,485 \text{ C mol}^{-1}$]	v	fluid velocity [m s^{-1}]
f	friction factor [–]	V	volume [m^3]
\bar{g}_m	mass transport coefficient [m s^{-1}]	\bar{X}	species mole fraction ($\text{H}_2, \text{H}_2\text{O}, \text{N}_2, \text{O}_2$) [–]
g	gravitational acceleration [m s^{-2}]		
h	enthalpy [kJ kmol^{-1}], convective heat transfer coefficient [$\text{kW m}^{-2} \text{K}^{-1}$]	<i>Greek letters:</i>	
h_f	head loss [–]	ϕ	species diffusion flux between GDL and bulk gases ($\text{H}_2, \text{H}_2\text{O}, \text{N}_2, \text{O}_2$) [kmol s^{-1}]
ΔH	enthalpy of formation [kJ mol^{-1}]	α	transfer coefficient [–]
i_0	exchange current density [A m^{-2}]	ε	porosity of GDL [–]
I	electrical current [A]	κ	ionic conductivity [S m^{-1}]
k_f	fluid conduction heat transfer coefficient [$\text{kW m}^{-1} \text{K}^{-1}$]	ρ	density [kg m^{-3}]
k_s	solid conduction heat transfer coefficient [$\text{kW m}^{-1} \text{K}^{-1}$]	σ	electrode conductivity [S m^{-1}]
L	length [m]	<i>Superscripts and subscripts:</i>	
n	number of participating electrons in the reaction [–]	act	activation polarization
N	total number of moles [kmol]	GDL	gas diffusion layer
\dot{N}	molar flow rate [kmol s^{-1}]	g	bulk gas control volume
Nu_D	Nusselt number [–]	in	into control volume
P	pressure [kPa]	MEA	membrane electrode assembly
\dot{Q}	heat transfer [kW]	ohm	ohmic polarization
R	fuel cell external/load resistance [Ω]	out	out of control volume
		ref	reference condition
		s	solid control volume
		0	standard condition

Even though the HT-PEMFC has many attractive features, only a few studies on HT-PEMFCs have been performed. In particular, many modeling efforts over the last 20 years have focused on typical PEMFCs with a Nafion® membrane [20–24]; however, research on HT-PEMFCs with a PBI membrane began approximately five years ago and there remains a lack of modeling work. Only several steady-state models for the HT-PEMFC have been reported [14,25–31]. Cheddie and Munroe [25–27] were the first authors to develop a model of the HT-PEMFC. They developed the one-, two- and three-dimensional models. These models could predict the oxygen depletion occur in the cathode catalyst layer and a temperature rise of up to 20 K at a power density of 1000 W m^{−2}. Peng and Lee [14] developed a three-dimensional non-isothermal numerical model with a computational fluid dynamics (CFD) code and they found that thermal effects strongly affect the fuel cell performance. Scott et al. [28] developed a steady-state isothermal one-dimensional model which considered the effect of water transport across the membrane on the conductivity of the PBI membrane. Ubong et al. [29] conducted both experimental work and numerical simulations. A single cell with an active area of 45 cm² and with triple serpentine flow channels was used in the experiment. The crossover of reactant gases through the membrane was solved analytically by Shamardina et al. [30] with a pseudo two-dimensional steady-state isothermal model. Lobato et al. [31] developed a three-dimensional model that was solved for three different flow channel geometries. The results showed that serpentine flow channels achieved the best performance. In addition to these steady-state models, a few dynamic models for HT-PEMFCs were published. Zenith et al. [33] developed a dynamic model using the characteristic of cell resistance as an input. Peng

et al. [34] improved upon the previous model [14] with an accumulation (unsteady) term and observed the influence of the charge double-layer effect. Sousa et al. [35] developed a dynamic two-dimensional non-isothermal model and simulated the transient response. They observed the double-layer effect and degradation effect of phosphoric acid loss from the catalyst layers and platinum sintering in the cathode catalyst layer. Additionally, they reported on the transient response of the oxygen mole fraction and the temperature of the membrane electrode assembly (MEA).

The models that have been developed have limitations. First, the active area of the MEA is small (less than 10 cm²). With this lab-scale MEA size, previous models could not capture the local characteristics of the HT-PEMFC. Consideration of the local distribution is important because the variations in the local characteristics of a fuel cell may cause detrimental effects on the performance and lifespan of the fuel cell. Second, most of the models only address the steady-state characteristics. To understand the transient behavior – such as system start-up, shutdown and rapid changes in power demand – a dynamic model is essential. In fact, the models based on CFD may not be manageable or suitable for predicting the dynamic behavior and developing a control system because they require large computing resources and have a long computational time.

The objective of this work is to develop a quasi-three-dimensional non-isothermal dynamic model of an HT-PEMFC with a phosphoric acid-doped PBI membrane. This work is the only attempt so far to develop a model of an HT-PEMFC in a quasi-three-dimensional geometry. The advantage of the model is that it is simpler in geometry compared to the three-dimensional models using CFD codes; therefore, it is possible to capture local

distributions of temperature, current density and species mole fractions in a short time. The calculation time was 123 s for the model to simulate 500 s in real time using an Intel® Core™ Duo Processor at 2.80 GHz (Intel Corporation, Santa Clara, CA, USA) with 3.50 GB RAM. Because the model has an active area of 50 cm², it is possible to consider meaningful simulation results of local distributions. In addition, this model can be used to capture dynamic responses during a step change in current and to elucidate which element could affect the transient response by considering the simulation results from the transient state. Furthermore, because the model is implemented using MATLAB®-Simulink® (MathWorks, Inc., Natick, MA, USA), it can be used to develop and test control strategies. This model could also be expanded to include integrated fuel cell systems. Consequently, this model can be useful for the development of control strategies for enhancing overall HT-PEMFC system performance.

2. Model description

In this work, a dynamic non-isothermal quasi-three-dimensional model of an HT-PEMFC with a PBI membrane is developed. The unit cell is discretized in the stream-wise direction (x , y) and in the cross-sectional direction (z). By this method, the three-dimensional geometry of the model can be simplified (2+1D, quasi-3D). As shown in Fig. 1, the unit cell is discretized along the cross-sectional direction (z) into nine control volumes, which consist of the following: (1) the solid plate, (2) the bulk gas, (3) the GDL, (4) the MEA and (5) the coolant. These control volumes are needed to understand the energy and the mass transport of local sections of the cell in the cross-sectional direction. In addition to this discretization, the unit cell is also discretized in the stream-wise direction. One set of the nine control volumes in the cross-sectional direction is repeated in the stream-wise direction. This allows the model to capture the serpentine flow pattern, and the distributions of current density, temperature and species

Table 1

Geometrical HT-PEMFC model parameter values.

Description geometry	Value	Units
Cell width (x)	0.07	m
Cell height (y)	0.07	m
Depth of anode gas channel (z)	0.0015	m
Depth of cathode gas channel (z)	0.0015	m
Thickness of GDL (z)	0.0003	m
Thickness of electrolyte (z)	7×10^{-5}	m
Thickness of separator plates (z)	0.002	m

concentrations. As shown in Fig. 1, the model contains 25 sets of control volumes repeated along the stream-wise direction, which represent 4-step serpentine flow channels. These 25 sets of control volumes (a total of 225 control volumes) are enough to capture the local characteristics of a PEMFC [20,21]. The axial heat transfer network is considered within these repeated control volumes. Tables 1 and 2 show the geometrical and general model parameter values, respectively.

2.1. Assumptions

The major assumptions that are adopted in the model are the same as that of Mueller et al.'s work [20]. In HT-PEMFCs, the water in the cell exists only in the vapor phase, so a single-phase flow is also assumed [27]. The water drag coefficient from anode to cathode is assumed to be zero because of the property of the PBI membrane [29]. Additionally, the PBI membrane is assumed to be impermeable to gas flow [27].

2.2. Conservation equations

The cell characteristics – such as temperature, species mole fractions, and molar flow rate of each control volume – are solved from the conservation equations [20,21]. In addition, in the present work, some equations are modified to adopt the characteristics of HT-PEMFCs. Energy conservation and heat transfer equations are used to solve the temperature, and the species conservation and mass transport equations are used to solve the species mole fractions and the molar flow rates. These equations are described and given in the following sections (2.2.1., 2.2.2.).

Table 2

General HT-PEMFC model parameter values for the validation and the base case.

Description	Value	Units
Transfer coefficient	1	–
GDL porosity	0.4	–
Cell temperature	423	K
Anode stoichiometric mass flow rate (H ₂)	1.5	–
Cathode stoichiometric mass flow rate (air)	2.0	–
Coolant inlet temperature	423	K
Coolant outlet temperature	393 for validation 425 @ 0.7 A cm ⁻² 394 @ 0.4 A cm ⁻² for validation	K
Anode/cathode outlet pressure	101.325	kPa
Cathode reference exchange current density	1.78×10^{-6}	A m ⁻²
$T_{ref,i}$	353	K
E_a^0/R	16,456	K
Electrolyte reference conductivity	1.87	S m ⁻¹
$T_{ref,c}$	423	K
E_a^c/R	4549.3	K
GDL conductivity	570	S m ⁻¹

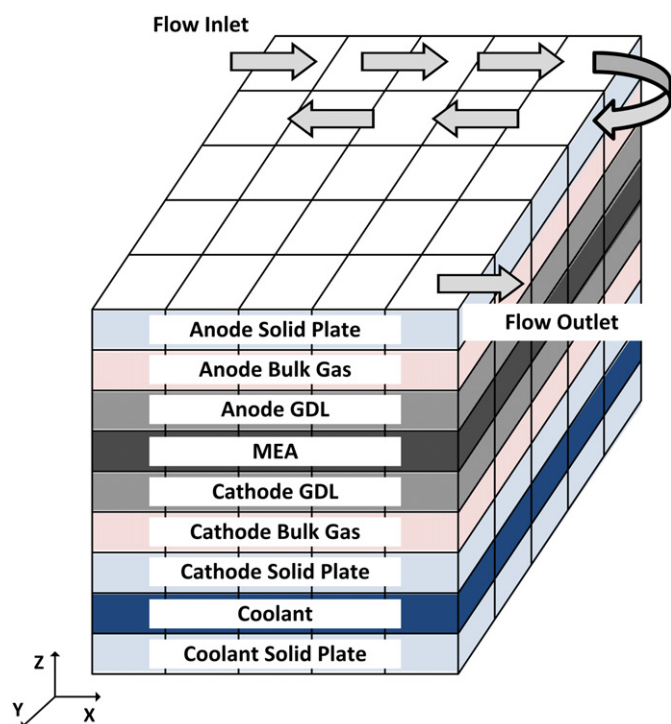


Fig. 1. Illustration of the stream-wise and the cross-sectional discretizations of an HT-PEMFC.

2.2.1. Energy conservation

To determine the temperature within the control volumes, energy conservation equations are solved. The temperatures of each solid plate control volume are determined by solving the following ordinary differential equation (ODE):

$$\rho VC \frac{dT}{dt} = \sum \dot{Q}_{in} \quad (1)$$

where \dot{Q}_{in} represents heat transfer from each of the control volumes. In a similar way, the bulk gas and the coolant temperature are determined by solving the following energy equation:

$$NC_v \frac{dT}{dt} = \sum \dot{N}_{in} h_{in} - \sum \dot{N}_{out} h_{out} + \sum \dot{Q}_{in} \quad (2)$$

$\dot{N}_{in} h_{in}$ and $\dot{N}_{out} h_{out}$ in Eq. (2) are used to determine the change in the enthalpy flux. The first term represents the enthalpy flux into the control volume and the second term represents the enthalpy flux out of the control volume.

In the model, the temperature of the control volume is taken to be the outlet temperature of the control volume and this outlet temperature is taken to be the inlet temperature of the next control volume in the stream-wise direction. Because the GDL and the MEA are assumed to have a lumped temperature, the temperature of the GDL and MEA is found by combining the gas and solid control volume conservation equations. Furthermore, heat generation from the electrochemical reactions is modeled as follows:

$$\left(\sum (\rho VC)_s + \sum (NC_v)_g \right) \frac{dT}{dt} = \sum \dot{N}_{in} h_{in} - \sum \dot{N}_{out} h_{out} + \sum \dot{Q}_{in} + \Delta H \cdot \frac{I}{nF} - \frac{V \cdot I}{1000} \quad (3)$$

where ΔH is the enthalpy of the formation of water, and V and I are the fuel cell voltage and current, respectively.

2.2.2. Species conservation

The species molar flow rates and species mole fractions at each control volume exit are determined from species mass conservation. The exit mole number of each bulk gas control volume is found from the species conservation equation:

$$\frac{d(N\vec{X})}{dt} = \dot{N}_{in} \vec{X}_{in} - \dot{N}_{out} \vec{X}_{out} + \sum \vec{\Phi} \quad (4)$$

The exit molar flow rate is determined from the total species conservation equation:

$$\dot{N}_{out} = \dot{N}_{in} + \sum \vec{\Phi} - \sum \frac{d(N\vec{X})}{dt} \quad (5)$$

$\vec{\Phi}$ in Eqs. (4) and (5) is the species diffusion flux from the adjacent GDL control volume. The “perfectly stirred” assumption [20] is applied to all control volumes in the model to solve the exit mole fraction and the molar flow rate. The control volume’s mole fractions are assumed to be those at the control volume exits.

The species mole number of each GDL control volume is determined as follows:

$$\frac{d\vec{N}}{dt} = - \sum \vec{\Phi} + \vec{R} \quad (6)$$

where \vec{R} is the local electrochemical reaction rate for each species. Because there is no water transport across the membrane, the water flux from the MEA is ignored.

2.3. Heat transfer

Because heat is generated in the fuel cell due to irreversibility in the electrochemical reactions, the extant heat transfer between adjacent control volumes ($\sum \dot{Q}_{in}$) in Eqs. (1)–(3) needs to be defined. The heat generated from the MEA control volume is transferred to the bulk gas through convection heat transfer. In addition, some amount of heat from the MEA control volume is also transferred to the solid plate through conduction. The heat in the solid plate is then transferred to the coolant channel (in the case of a cathode solid plate) or ambient air (in the case of an anode solid plate) through convection. Furthermore, some amount of heat from the solid plate is transferred to the bulk gas because the solid plate is in thermal contact with the bulk gas. In addition to these heat transfers in the perpendicular direction, heat is transferred between repeated control volumes along the in-plane direction. Specifically, conduction heat transfer between adjacent solid plates and natural convection at the edge of each plate are included in the model.

Convection heat transfer between a solid and a gas is determined by Newton’s law of cooling:

$$\dot{Q} = A \cdot h (T_2 - T_1) \quad (7)$$

Conduction heat transfer is determined by Fourier’s law:

$$\dot{Q} = \frac{A \cdot k_s (T_2 - T_1)}{L} \quad (8)$$

2.4. Reaction rates and species diffusion

Reaction rates, \vec{R} , and species diffusion, $\vec{\Phi}$, in the mass conservation equations (Eqs. (4)–(6)) are resolved in the model.

From Faraday’s law, the reaction rates of both half-reactions are a function of the current as follows:

$$\dot{R}_{H_2O} = -\dot{R}_{H_2} = -2\dot{R}_{O_2} = \frac{I}{n \cdot F} \quad (9)$$

Species diffusion is considered between the bulk gas and GDL control volumes. The driving force of species transport from the bulk gas to the GDL is convection driven by a concentration gradient and diffusion in the GDL. The mass transport coefficient, \vec{g}_m , at the interface between the gas channel and the GDL is obtained based on the Reynolds analogy between heat and mass transfer:

$$\vec{g}_m = \frac{Sh \cdot \vec{D}_m}{D_H} \quad (10)$$

where Sh is the Sherwood number, \vec{D}_m is the diffusion coefficient and D_H is the hydraulic diameter of the gas flow channel. The diffusion coefficients for the species are determined by the temperature and the pressure. A modified diffusion coefficient, obtained from the Bruggeman correlation, is defined to account for the effects of porosity and tortuosity in the GDL:

$$\vec{D}_m = \vec{D}_0 \left(\frac{T}{T_0} \right)^{3/2} \left(\frac{P_0}{P} \right) \quad (11)$$

$$\vec{D}_m^{\text{eff}} = \varepsilon^{1.5} \cdot \vec{D}_m \quad (12)$$

where \vec{D}_0 is the species diffusion coefficient at standard pressure and temperature, \vec{D}_m^{eff} is the effective species diffusion coefficient

and ε is the GDL porosity. The species diffusion flux between the bulk gas and the GDL is the following:

$$\vec{R}_{\text{dif}} = A \cdot \frac{1}{\frac{1}{\vec{g}_m} + \frac{t_{\text{GDL}}}{D_m^{\text{eff}}}} \quad (13)$$

$$\vec{\Phi} = \vec{R}_{\text{dif}} \cdot (\vec{C}_2 - \vec{C}_1) \quad (14)$$

where \vec{R} is the total diffusion resistance of each species, and t_{GDL} is the thickness of the GDL.

2.5. Electrochemical model

The operating voltage of the cell is determined as follows:

$$V = V_{\text{Nernst}} - \eta_{\text{act}} - \eta_{\text{ohmic}} \quad (15)$$

where the Nernst voltage over 100 °C is determined based on the partial pressures in the GDL and on the MEA temperature [14]. The Nernst voltage is found by the following equation:

$$V_{\text{Nernst}} = E^0 + 4.308 \cdot 10^{-5} \ln \left[\frac{P_{\text{H}_2} \cdot (P_{\text{O}_2})^{0.5}}{P_{\text{H}_2\text{O}}} \right] \quad (16)$$

where

$$E^0 = 1.17 - 2.576 \cdot 10^{-4} (T - 373.15) \quad (17)$$

The exchange current density depends on the temperature according to the Arrhenius equation [31]:

$$i_0 = i_0^{\text{ref}} \exp \left[-\frac{E_a^i}{R} \left(\frac{1}{T} - \frac{1}{T_{\text{ref},i_0}} \right) \right] \quad (18)$$

where E_a^i is the activation energy and i_0^{ref} is the reference exchange current density at reference temperature T_0 . The activation polarization is modeled using the Tafel equation:

$$\eta_{\text{act}} = \frac{RT}{\alpha F} \ln \left(\frac{I/A}{i_0} \cdot \frac{C_{\text{O}_2}^{\text{ref}}}{C_{\text{O}_2}} \right) \quad (19)$$

The ionic conductivity of the PBI membrane is described by the Arrhenius equation [31]:

$$\kappa = \kappa_0 \exp \left[-\frac{E_a^k}{R} \left(\frac{1}{T} - \frac{1}{T_{\text{ref},\kappa}} \right) \right] \quad (20)$$

where E_a^k is the activation energy and κ_0 is the pre-exponential factor.

The cell resistance is modeled by the membrane ionic conductivity, κ , and the electrode electric conductivity, σ , and the ohmic polarization is proportional to the cell resistance:

$$R_{\text{ohmic}} = \frac{t_{\text{MEA}}}{\kappa} + \frac{2t_{\text{GDL}}}{\sigma} \quad (21)$$

$$\eta_{\text{ohmic}} = I \cdot R_{\text{ohmic}} \quad (22)$$

2.6. Pressure drop

The local pressures of the anode and the cathode channels were calculated to predict accurate local characteristics, such as the Nernst voltage. The pressure loss of the reactant gas flow due to the

cell length was considered. The Reynolds number was calculated to resolve the friction factor of each flow. When the flow had a Reynolds number under 2100, it was assumed to be laminar flow where the Laminar Friction Constant, f_{Re} , is 56.91 for a square or a rectangular flow geometry. The head loss can be calculated by Eq. (25) and the pressure drop can be described by Eq. (26). The following expressions define the Reynolds number, friction factor, head loss and pressure drop, respectively [32]:

$$\text{Re} = \frac{\rho v D_H}{\mu} \quad (23)$$

$$\text{Re} \leq 2100 \quad f = \frac{56.91}{\text{Re}} \quad (24)$$

$$h_f = f \frac{L}{D_H} \frac{v^2}{2g} \quad (25)$$

$$\Delta p = \rho g h_f \quad (26)$$

3. Results and discussion

3.1. Model validation

The polarization curve simulated in this model was compared with published experimental data [31]. Because the model in this paper was developed for a 4-step serpentine flow geometry, the experimental data for the same flow geometry were selected. Fuel cell geometric properties and conditions of the experimental work [31] are the same for those of the simulation work in this paper as shown in Tables 1 and 2. The operating temperature for the validation is 393 K, and stoichiometric mass flow ratio of anode (H_2) and cathode (air) is 1.5 and 2.0, respectively. Since the current simulation model in this paper is non-isothermal and, yet, there was no information about how large the temperature variation throughout the cell in the experimental work, thus it was assumed that there was a temperature difference of 1 K between the coolant inlet and the coolant outlet at the load current condition of 0.4 A cm⁻². Experimental and simulated polarization curves over the range of current densities from 0 to 0.4 A cm⁻² are shown in Fig. 2. The simulation results showed a good agreement with the experimental data whose error range is within 4%.

3.2. Steady results

3.2.1. Distribution of local characteristics

Because the model is intended to predict local characteristics such as current density, MEA temperature and species mole fraction, each distribution at an operating temperature of 423 K is shown in Figs. 3–5. These results were simulated at a high current density of 0.7 A cm⁻². The distribution of the current density and the MEA temperature were investigated with two different coolant outlet temperatures. With a changing coolant flow rate, in case 1, the coolant temperature difference between the inlet and the outlet was set to 2 K (423–425 K); in case 2, the coolant temperature difference was set to 7 K (423–430 K). Simulation results are explained below and summarized in Table 3.

3.2.1.1. Species mole fraction. The local hydrogen mole fraction at the anode was 1 in all areas because the cell was operating with pure, dry hydrogen and no water diffusion through the membrane. On the other hand, at the cathode, the oxygen and water mole fractions varied along the flow direction. Fig. 3 shows the distributions of the oxygen mole fraction of the cathode channel. The

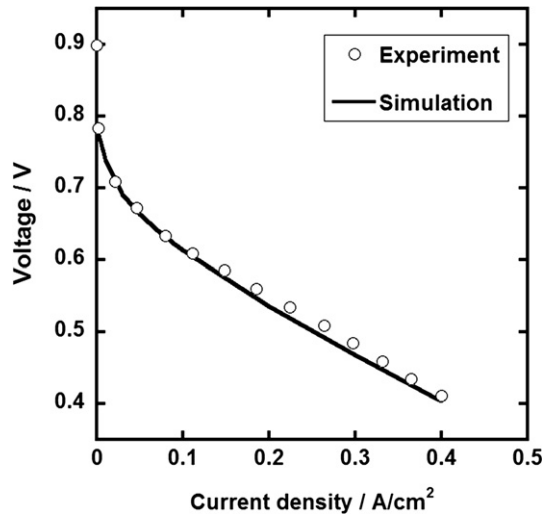


Fig. 2. Comparison of polarization curves between the experimental and the simulation data at a cell temperature of 393 K.

oxygen mole fraction at the cathode channel inlet before the entry was 0.21 and decreased along the cathode gas channel. The water mole fraction at the cathode channel inlet was nearly zero because of its no-humidification condition, and it increased along the cathode gas channel to 0.3. The tendency of the variation in the water mole fraction is opposite that of the oxygen mole fraction (Fig. 3). This variation is because oxygen is consumed by the electrochemical reaction and because two water molecules are produced for one oxygen molecule consumed. Thus, the water mole fraction increased while the oxygen mole fraction decreased along the cathode gas channel.

3.2.1.2. MEA temperature. The MEA temperature increased along the coolant channel as indicated in Fig. 4. The MEA temperature increased from 424.1 K (at the cathode inlet) to 425.8 K (at the cathode outlet) in case 1 and from 424.4 K to 431.1 K in case 2. As heat was generated by the cell, the heat was transferred to the coolant and the coolant temperature increased. Due to the increased coolant temperature, the amount of heat removal from the MEA to the coolant decreased along the coolant channel. This phenomenon resulted in an increase in the MEA temperature along the coolant channel. The amount of heat generated by the cell and

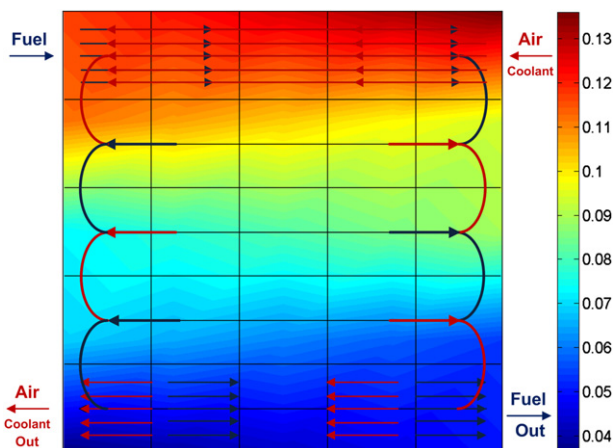


Fig. 3. The distribution of the oxygen mole fraction in a cathode channel at a cell operating temperature of 423 K and a cell current density of 0.7 A cm^{-2} .

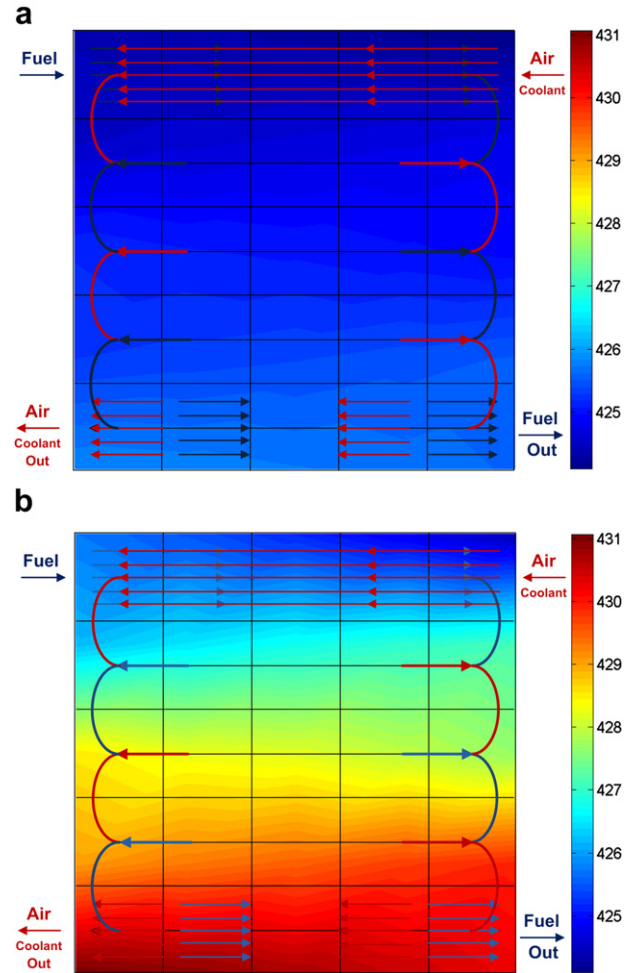


Fig. 4. The distribution of the MEA temperature (K) at a cell operating temperature of 423 K and a cell current density of 0.7 A cm^{-2} . a) Case 1; b) Case 2.

transferred to the coolant was 31.5 W and 26.26 W, respectively, for the heat transfer between the MEA and the coolant in case 1. In case 2, the amount of heat generated by the cell and transferred to the coolant was 30.7 W and 24.84 W, respectively.

3.2.1.3. Current density. The current density distributions for cases 1 and 2 are shown in Fig. 5. In case 1, the current density decreased along the cathode gas channel. The local current density at the cathode outlet (0.65 A cm^{-2}) was 11% lower than at the cathode inlet (0.73 A cm^{-2}) and the standard deviation of the current density of the entire area was 0.025 A cm^{-2} . This result was caused by a variation in the activation overvoltage. According to Eq. (19), there is an oxygen concentration term and the activation overvoltage increased while the oxygen concentration decreased along the cathode gas channel. There is also a temperature term, such as the MEA temperature and the exchange current density, in the activation overvoltage equation. Nevertheless, as described in the previous section (3.2.1.2.), the MEA temperature varied only 0.4% in case 1 and this change did not significantly affect the activation overvoltage. For the same reason, the membrane ionic conductivity varied slightly (1.922 S m^{-1} at the cathode inlet and 2.008 S m^{-1} at the cathode outlet). Thus, the ohmic resistance also varied slightly and this effect did not significantly affect the local current density.

Unlike case 1, in case 2, the standard deviation of the current density of the entire area was 0.009 A cm^{-2} and the local current density was quite uniform compared to case 1. In contrast to the

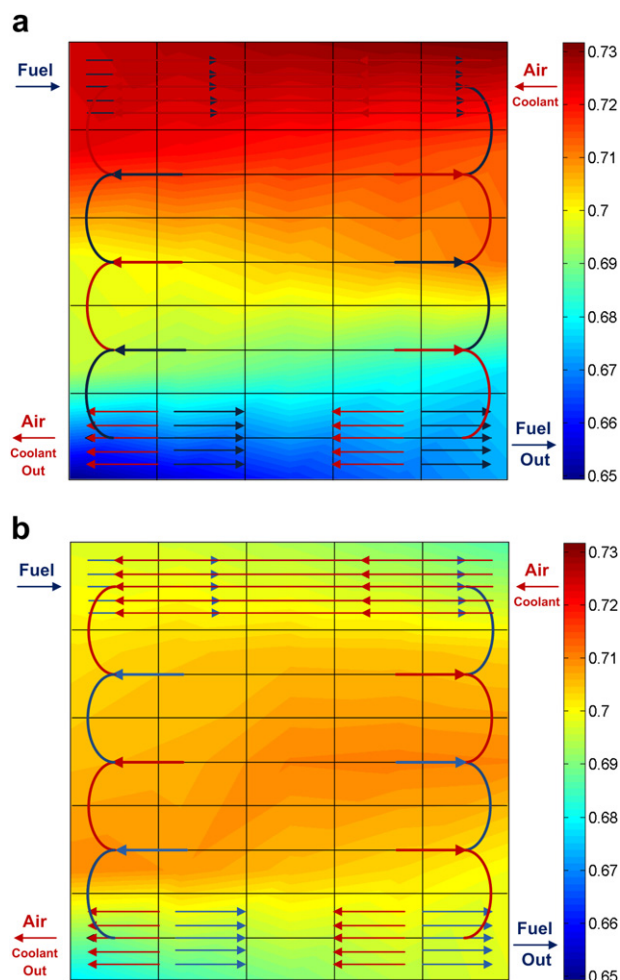


Fig. 5. The distribution of the current density (A cm^{-2}) at a cell operating temperature of 423 K and a cell current density of 0.7 A cm^{-2} . a) Case 1; b) Case 2.

results of case 1, the temperature influence was also significant for the local current density due to the temperature variance throughout the cell. Specifically, the membrane ionic conductivity increased along the cathode gas channel (1.938 S m^{-1} at the cathode inlet and 2.287 S m^{-1} at the cathode outlet). This result is because the ionic conductivity of the PBI membrane is dependent on temperature, as demonstrated in Eq. (20), and the ionic conductivity is proportional to the MEA temperature. Thus, the local ohmic resistance in the cell, which is strongly dependent upon the membrane ionic conductivity, decreases as the MEA temperature increases. Consequently, a higher temperature improves the

local current density. Additionally, in the activation overvoltage, the exchange current density term increases as the MEA temperature increases as in Eq. (18). This effect could reduce the activation overvoltage along the cathode gas channel, which was increased by the concentration effect, as the results of case 1 demonstrate. Thus, increasing temperature enhances fuel cell performance.

3.3. Dynamic results

3.3.1. Cell voltage changes

The transient response of the voltage when a step change in the current density was applied to the model is shown in Fig. 6. The current density was instantaneously increased from 0.4 A cm^{-2} to 0.8 A cm^{-2} at 500 s and, then, instantaneously decreased from 0.8 A cm^{-2} to 0.4 A cm^{-2} at 700 s. (The mass flow rates of the reactant gases were changed immediately by a corresponding amount when a step change in the current density was applied.) Undershoot and overshoot occurred in the voltage in response to the step changes in the current density. When the current density was changed from 0.4 A cm^{-2} to 0.8 A cm^{-2} , the voltage rapidly decreased from 0.48 V to 0.3 V. Then, the voltage increased to its steady-state value of 0.33 V. When the current density was changed from 0.8 A cm^{-2} to 0.4 A cm^{-2} , the voltage suddenly increased from 0.33 V to 0.5 V and, then, settled to its steady-state value of 0.48 V. These results were calculated under the condition at which coolant outlet temperature is 432 K at the second steady-state (after current step-up from 0.4 A cm^{-2} to 0.8 A cm^{-2}) while the coolant inlet temperature is 423 K and the coolant flow rate is kept constant despite the change in the load. Table 4 shows simulation conditions and results of cell voltage changes.

To elucidate the voltage transient behavior, especially the undershoot phenomenon, the transient responses of the average oxygen mole fraction and the average MEA temperature during the current step-up were considered. The transient response of the average oxygen mole fraction in the catalyst layer during the load change is shown in Fig. 7(a). When the load was changed from 0.4 A cm^{-2} to 0.8 A cm^{-2} , the oxygen mole fraction decreased smoothly from 0.1119 to 0.0741 within 0.5 s. These results can be explained by the following phenomenon: an excess of oxygen in the catalyst layer was consumed immediately after the load changed and the change in the local oxygen concentration was delayed because the oxygen diffusion cannot follow the change in

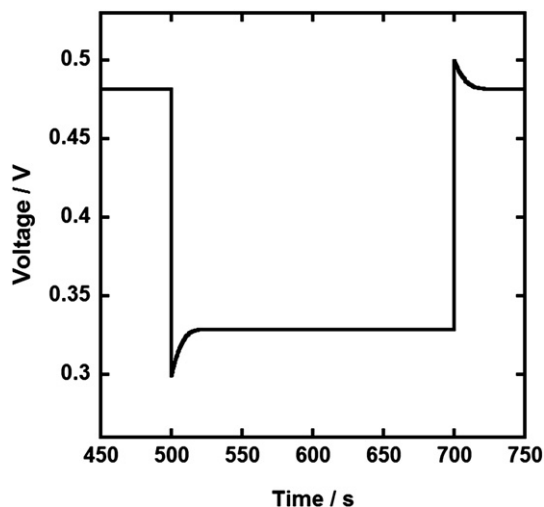


Fig. 6. Transient response of voltage as the current density changes from 0.4 A cm^{-2} to 0.8 A cm^{-2} at 500 s and from 0.8 A cm^{-2} to 0.4 A cm^{-2} at 700 s.

Table 3
Simulation results of the steady-state.

Description	Value		Units
	Case 1	Case 2	
Load current	0.7		A cm^{-2}
Operating temperature	423		K
Coolant inlet temperature	423		K
Coolant outlet temperature	425	430	K
MEA temperature (cathode inlet)	424.1	424.4	K
MEA temperature (cathode outlet)	425.8	431.1	K
Membrane ionic conductivity (cathode inlet)	1.922	1.938	S m^{-1}
Membrane ionic conductivity (cathode outlet)	2.008	2.287	S m^{-1}
Standard deviation of current density	0.025	0.009	A cm^{-2}

Table 4
Simulation results of the transient state.

Description		Value	Units
Current step	@ 500 s	0.4–0.8	A cm^{-2}
	@ 700 s	0.8–0.4	
Coolant inlet temperature		423	K
Coolant outlet temperature	@ 1st steady-state	426	K
	@ 2nd steady-state	432	
	@ 3rd steady-state	426	
Steady-state value	@ 1st steady-state	0.48	V
	@ 2nd steady-state	0.33	
	@ 3rd steady-state	0.48	

current density instantaneously [26]. This phenomenon resulted in variations in the open-circuit voltage and the activation overvoltage. As described in Eqs. (16) and (19), the open-circuit voltage and the activation overvoltage depend on the oxygen mole fraction at the cathode catalyst layer.

The transient response of the average MEA temperature, when the load current was changed from 0.4 A cm^{-2} to 0.8 A cm^{-2} , is shown in Fig. 7(b). The MEA temperature gradually increased from 425.09 K to 429.17 K within 25 s. In fuel cells, the electrochemical

reaction is more active in the high current density area and the more active the electrochemical reaction is, the more heat is released from the cell. Thus, the temperature increased during the step load change. Furthermore, the temperature reached the steady-state value after a few tens of seconds and this caused a time delay in reaching the steady state in some of the variables that are a function of temperature. Specifically, the activation overvoltage and the ohmic overvoltage, which directly affect the I–V curves of the fuel cell, varied with the step load change.

The changes of the activation overvoltage and the ohmic overvoltage, when a step change in the current density from 0.4 A cm^{-2} to 0.8 A cm^{-2} occurred, are shown in Fig. 8. The open-circuit voltage was varied by only 0.04% before and after the step change in the current density, thus it is not considered in Fig. 8. As shown in Fig. 8, when the step change in the current density occurred, the activation overvoltage and the ohmic overvoltage showed somewhat different responses that the overvoltage reached their highest value during the overshoot period. The activation overvoltage, which is affected by both the oxygen mole fraction and the MEA temperature, reached the highest value of 0.568 V at 0.3 s after the step change in the current density while the ohmic overvoltage, which is affected by the MEA temperature, reached the highest value of 0.292 V just after the step change in the current density without any delay. After that, two overvoltages reached their steady-state

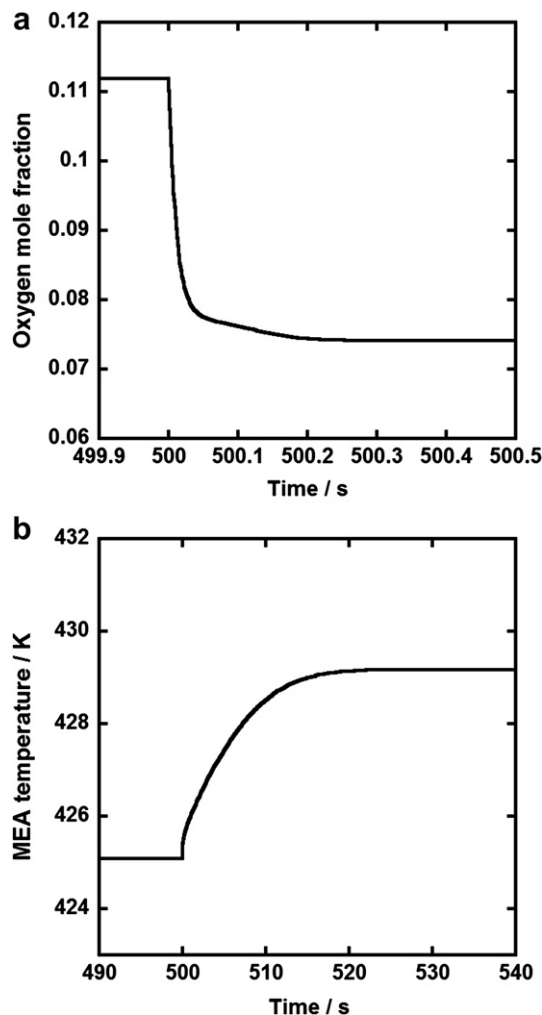


Fig. 7. Transient responses of the oxygen mole fraction and the MEA temperature at cathode catalyst layer as the current density changes from 0.4 A cm^{-2} to 0.8 A cm^{-2} at 500 s a) oxygen mole fraction; b) MEA temperature.

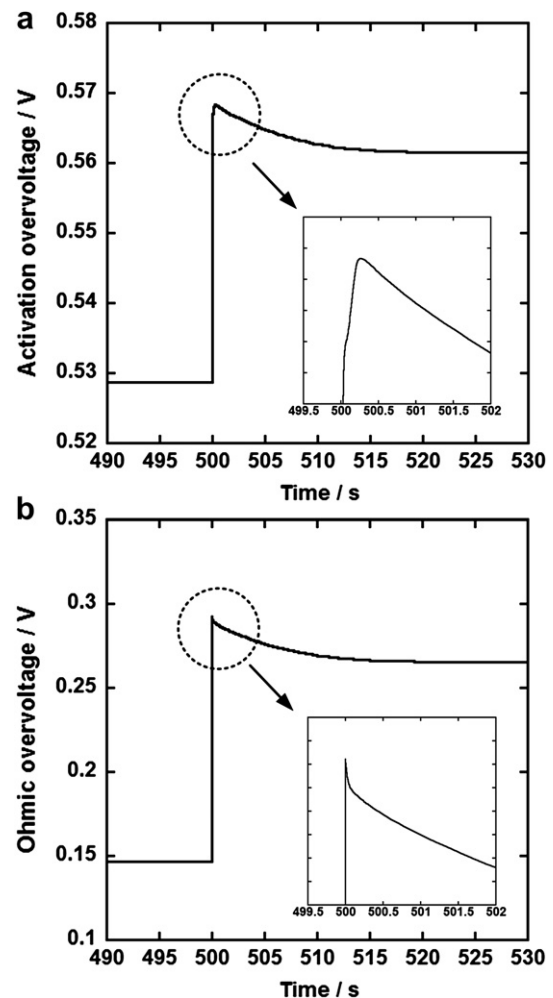


Fig. 8. Transient responses of the activation overvoltage and the ohmic overvoltage as the current density changes from 0.4 A cm^{-2} to 0.8 A cm^{-2} at 500 s a) activation overvoltage; b) ohmic overvoltage.

value within a few tens of seconds. These behaviors confirm that the effect of the oxygen mole fraction and the MEA temperature on the overvoltage responses when a step change in the current density occurred. As described above, the transient response of oxygen mole fraction affects the transient response of the activation overvoltage in the early stage (within a few tenths of seconds) and the transient response of MEA temperature affects the activation overvoltage and the ohmic overvoltage in the late stage (within a few tens of seconds). Consequently, the transient response of voltage is affected by the oxygen mole fraction in the early stage and the MEA temperature in the late stage.

The tendencies of the transient responses of the oxygen mole fraction and the MEA temperature were also reported by Sousa et al. [35]. They reported that the time to reach steady-state was within 0.15 s for the oxygen mole fraction and 200 s for the MEA temperature. Although the time to reach the steady-state value of the MEA temperature is somewhat different from this work, it is important that the MEA temperature did not reach the steady-state value as fast as the oxygen mole fraction. Additionally, this tendency was compared with that of typical PEMFCs as reported by Cho et al. [36]. They demonstrated that there are two different time delays in the transient response of the cell voltage when a step load change occurs. The first time delay is the time over which the voltage decreases until it reaches the minimum level due to the time needed for oxygen to penetrate the GDL. The second time delay is due to membrane water content recovery which is related to the membrane ionic conductivity. In HT-PEMFCs, there were also two different time delays but the reason for the second time delay differed from typical PEMFCs. The second time delay in HT-PEMFCs is due to the time needed to reach the next steady-state value of the MEA temperature which is related to the membrane ionic conductivity. Consequently, to maintain performance during the transient state, it is important for an HT-PEMFC to have its cell temperature reach the next steady-state value quickly. This is in contrast to a typical PEMFC in which it is important to recover membrane water content quickly to maintain performance.

3.3.2. Temperature influence

The transient response results of the voltage with different coolant outlet temperatures are shown in Fig. 9. There are three cases that control the degree to which the temperature rises in

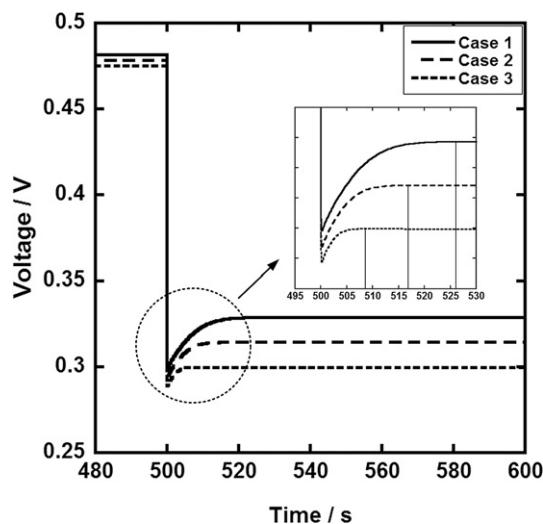


Fig. 9. Transient responses of voltage with different coolant outlet temperatures as the current density changes from 0.4 A cm^{-2} to 0.8 A cm^{-2} at 500 s.

Table 5

Simulation results of the transient state with different coolant outlet temperatures.

Description	Value			Units
	Case 1	Case 2	Case 3	
Current step		0.4–0.8		A cm^{-2}
Coolant inlet temperature		423		K
Coolant outlet temperature	432	429	426	K
Steady-state value	0.33	0.31	0.3	V
Time to reach steady-state	26	17	8	s

response to changes in the coolant flow rate. (Once the coolant flow rate was determined in each case, it did not change despite the change in the load.) Case 1 shows the greatest difference, 9 K, and case 2 and case 3 show differences of 6 K, and 3 K, respectively, where the coolant inlet temperature is 423 K. Table 5 shows these simulation conditions. When the current density was changed from 0.4 A cm^{-2} to 0.8 A cm^{-2} , case 1 showed the best steady-state performance of 0.33 V; however, the time to reach the steady state, 26 s, was the longest among the cases. Case 2 showed a steady-state performance of 0.31 V and a time delay of 17 s. Case 3 showed the worst steady-state performance, 0.3 V; however, the time to reach the steady state, 8 s, was the shortest among the cases. These results indicate that the transient response of the voltage in the HT-PEMFC is strongly dependent on cell temperature. To verify this, the transient response of the average MEA temperature to the coolant outlet temperature was plotted and is shown in Fig. 10. When the step load change occurred, the temperature gradually increased to the next state within a few tens of seconds and the time duration increased with the coolant outlet temperature. Furthermore, as the temperature reached the steady-state value after a few tens of seconds, this caused a time delay in reaching the steady state in some of the variables that are a function of temperature. The activation overvoltage and the ohmic overvoltage, which directly affect the I–V curves of the fuel cell, varied with the step load change. Fig. 11 shows the variations of the activation overvoltage and the ohmic overvoltage. When the cell current was increased, both the activation overvoltage and the ohmic overvoltage increased rapidly and decreased to the next steady state over a few tens of seconds. These results indicate why the transient response of the voltage varied with different coolant outlet temperatures.

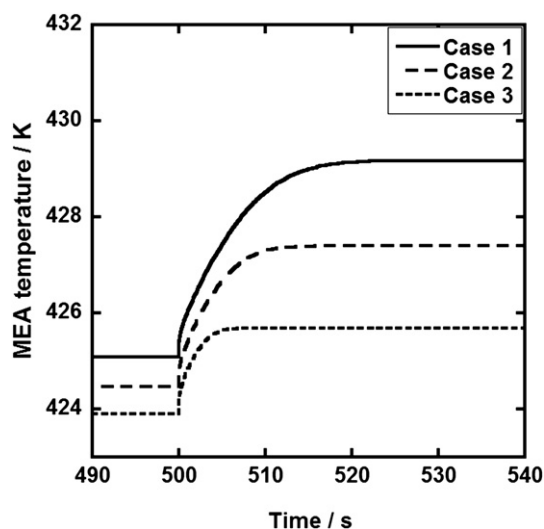


Fig. 10. Transient responses of the MEA temperature as the current density changes from 0.4 A cm^{-2} to 0.8 A cm^{-2} at 500 s.

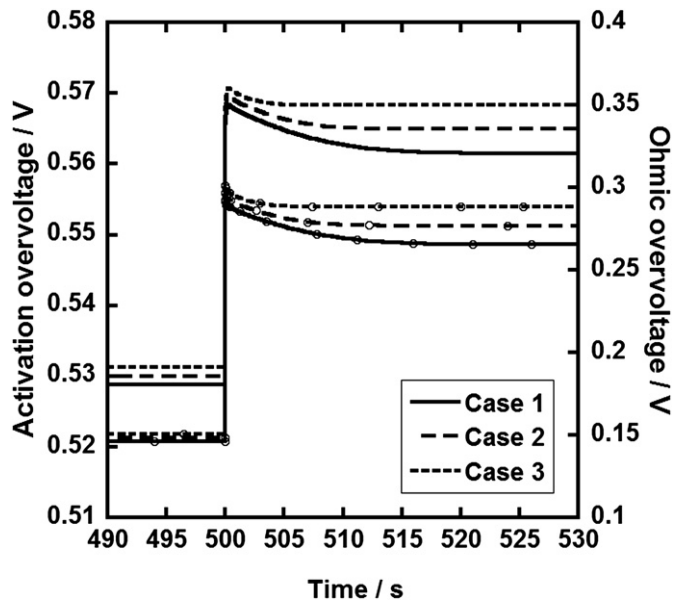


Fig. 11. Transient responses of the activation overvoltage and the ohmic overvoltage (lines with circles) with different coolant outlet temperatures as the current density changes from 0.4 A cm^{-2} to 0.8 A cm^{-2} at 500 s.

4. Conclusions

A dynamic non-isothermal quasi-three-dimensional model of a high-temperature PEMFC with a PBI membrane has been developed and simulated at various operating conditions in both steady-state and transient conditions.

The model is developed using the MATLAB®-Simulink® programming environment. The model is based on the dynamic equations of mass and energy conservation, mass and heat transfer and electrochemical reaction. The model consists of control volumes that are introduced in both the cross-sectional direction and the stream-wise direction. With these control volumes, the model can predict the HT-PEMFC characteristics. Specifically, the model can capture distributions of local current density, temperature, and species concentrations within a few minutes without using a CFD program. To validate the model, the polarization curve of the simulation data is compared to that of experimental data from the literature and the curve shows a good agreement with the experimental data.

The simulation results of the steady-state condition showed that there is a strong relationship between the local current density and the local MEA temperature. The activation overvoltage increases due to oxygen depletion along the cathode gas channel and this causes a reduction in current density. The rise in temperature through the cell can be controlled by changing the coolant flow rate and a higher temperature enhances membrane ionic conductivity. In that case, the ohmic resistance decreases and the current density increases. These trade-off relationships maintain uniform fuel cell performance.

The dynamic results indicate that when the current is instantaneously increased and decreased, a voltage undershoot and overshoot phenomenon is found. This undershoot and overshoot behavior is the result of delays: a delay in the local oxygen concentration because the oxygen diffusion cannot follow the change in current density instantaneously and a delay in the MEA temperature reaching the steady-state value. The time delay due to oxygen depletion is on the order of 0.1 s but for the case of the MEA

temperature, the delay time is on the order of 10 s. These results indicate that the transient response of voltage on the HT-PEMFC is strongly dependent on cell temperature.

Because the model can predict dynamic variations of characteristics related to fuel cell performance for various operating conditions with fast simulation times, it may be useful for the development of optimal control strategies for enhancing HT-PEMFC performance. In the future, the model can be expanded to include the integrated fuel cell system.

Acknowledgments

This work was supported by a grant from the Korea Government Ministry of Knowledge Economy, Brain Korea 21 (BK21) and KOSEF/SNU-IAMD.

References

- [1] S. Srinivasan, R. Mosdale, P. Stevens, C. Yang, *Annu. Rev. Energy Environ.* 24 (1999) 281–328.
- [2] G. Alberti, M. Cassiola, L. Massinelli, B. Bauer, *J. Membr. Sci.* 185 (2001) 73–81.
- [3] C. Yang, P. Costamagna, S. Srinivasan, J. Benziger, A.B. Bocarsly, *J. Power Sources* 103 (2001) 1–9.
- [4] P. Costamagna, C. Yang, A.B. Bocarsly, S. Srinivasan, *Electrochim. Acta* 47 (2002) 1023–1033.
- [5] I. Honma, H. Nakajima, S. Nomura, *Solid State Ionics* 154 (2002) 707–712.
- [6] Q. Li, R. He, J.O. Jensen, N.J. Bjerrum, *Chem. Mater.* 15 (2003) 4896–4915.
- [7] S.H. Kwak, T.H. Yang, C.S. Kim, K.H. Yoon, *Solid State Ionics* 160 (2003) 309–315.
- [8] N.H. Jalani, K. Dunn, R. Datta, *Electrochim. Acta* 51 (2005) 553–560.
- [9] Y. Song, J.M. Fenton, H.R. Kunz, L.J. Bonville, M.V. Williams, *J. Electrochem. Soc.* 152 (2005) A539–A544.
- [10] L. Qingfeng, H.A. Hjuler, N.J. Bjerrum, *J. Appl. Electrochem.* 31 (2001) 773–779.
- [11] J.A. Asensio, S. Borros, P.G. Romero, *J. Electrochem. Soc.* 151 (2004) A304–A310.
- [12] Q. Li, R. He, J.O. Jensen, N.J. Bjerrum, *Fuel Cells* 4 (2004) 147–159.
- [13] J.T. Wang, R.F. Savinell, J. Wainright, M. Litt, H. Yu, *Electrochim. Acta* 41 (1996) 193–197.
- [14] J. Peng, S.J. Lee, *J. Power Sources* 162 (2006) 1183–1191.
- [15] S.R. Samms, S. Wasmus, R.F. Savinell, *J. Electrochem. Soc.* 143 (1996) 1225–1232.
- [16] D. Weng, J.S. Wainright, U. Landau, R.F. Savinell, *J. Electrochem. Soc.* 143 (1996) 1260–1263.
- [17] Q. Li, R. He, J.A. Gao, J.O. Jensen, N.J. Bjerrum, *J. Electrochem. Soc.* 150 (2003) A1599–A1605.
- [18] J.O. Jensen, Q. Li, R. He, C. Pan, N.J. Bjerrum, *J. Alloys Compd* 404–406 (2005) 653–656.
- [19] J.O. Jensen, Q. Li, C. Pan, A.P. Vestbo, K. Mortensen, H.N. Petersen, et al., *Int. J. Hydrogen Energy* 32 (2007) 1567–1571.
- [20] F. Mueller, J. Brouwer, S. Kang, H.S. Kim, K. Min, *J. Power Sources* 163 (2006) 814–829.
- [21] S. Kang, K. Min, F. Mueller, J. Brouwer, *Int. J. Hydrogen Energy* 34 (2009) 6749–6764.
- [22] S.A. Freunberger, M. Santis, I.A. Schneider, A. Wokaun, F.N. Buchi, *J. Electrochem. Soc.* 153 (2006) A396–A405.
- [23] M.R. Andrew, in: K.R. Williams (Ed.), *An Introduction to Fuel Cells*, Elsevier Publishing Company, New York, 1966.
- [24] S. Choi, K. Chu, J. Ryu, M. Sunwoo, *Int. J. Automotive Technol.* 10 (2009) 719–732.
- [25] D. Cheddie, N. Munroe, *J. Power Sources* 156 (2006) 414–423.
- [26] D.F. Cheddie, N.D. Munroe, *Int. J. Transport Phenom.* 32 (2006) 832–841.
- [27] D.F. Cheddie, N.D. Munroe, *J. Power Sources* 160 (2006) 215–223.
- [28] K. Scott, S. Pilditch, M. Mamlouk, *J. Appl. Electrochem.* 37 (2007) 1245–1259.
- [29] E.U. Ubong, Z. Shi, X. Wang, *J. Electrochem. Soc.* 156 (2009) B1276–B1282.
- [30] O. Shamardina, A. Chertovich, A.A. Kulikovskiy, A.R. Khokhlov, *Int. J. Hydrogen Energy* 35 (2010) 9954–9962.
- [31] J. Lobato, P. Canizares, M.A. Rodrigo, F.J. Pinar, E. Mena, D. Ubeda, *Int. J. Hydrogen Energy* 35 (2010) 5510–5520.
- [32] F.M. White, *Fluid Mechanics*, fifth ed. McGraw-Hill, New York, 2003.
- [33] F. Zenith, F. Seland, O.E. Kongstein, B. Borresen, R. Tunold, S. Skogestad, *J. Power Sources* 162 (2006) 215–227.
- [34] J. Peng, J.Y. Shin, T.W. Song, *J. Power Sources* 179 (2008) 220–231.
- [35] T. Sousa, M. Mamlouk, K. Scott, *Int. J. Hydrogen Energy* 35 (2010) 12065–12080.
- [36] J. Cho, H.S. Kim, K. Min, *J. Power Sources* 185 (2008) 118–128.